

pubs.acs.org/JACS Article

Mechanism-Guided Kinetic Analysis of Electrocatalytic Proton Reduction Mediated by a Cobalt Catalyst Bearing a Pendant Basic Site

Jaruwan Amtawong, Charlotte L. Montgomery, Gabriella P. Bein, Austin L. Raithel, Thomas W. Hamann, Chun-Hsing Chen, and Jillian L. Dempsey*



Cite This: J. Am. Chem. Soc. 2024, 146, 3742-3754



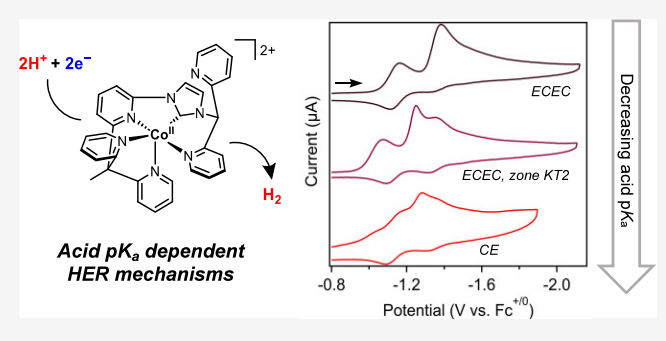
ACCESS I

III Metrics & More

Article Recommendations

Supporting Information

ABSTRACT: Cobalt polypyridyl complexes stand out as efficient catalysts for electrochemical proton reduction, but investigations into their operating mechanisms, with broad-reaching implications in catalyst design, have been limited. Herein, we investigate the catalytic activity of a cobalt(II) polypyridyl complex bearing a pendant pyridyl base with a series of organic acids spanning $20 \, \mathrm{pK_a}$ units in acetonitrile. Structural analysis, as well as electrochemical studies, reveals that the Co(III) hydride intermediate is formed through reduction of the Co(II) catalyst followed by direct metal protonation in the initial EC step despite the presence of the pendant base, which is commonly thought of as a more kinetically



accessible protonation site. Protonation of the pendant base occurs after the Co(III) hydride intermediate is further reduced in the overall ECEC pathway. Additionally, when the acid used is sufficiently strong, the Co(II) catalyst can be protonated, and the Co(III) hydride can react directly with acid to release H_2 . With thorough mechanistic understanding, the appropriate electroanalytical methods were identified to extract rate constants for the elementary steps over a range of conditions. Thermodynamic square schemes relating catalytic intermediates proposed in the three electrocatalytic HER mechanisms were constructed. These findings reveal a full description of the HER electrocatalysis mediated by this molecular system and provide insights into strategies to improve synthetic fuel-forming catalysts operative through metal hydride intermediates.

INTRODUCTION

Enabling efficient hydrogen production through the hydrogen evolution reaction (HER) is a promising pathway toward realizing a carbon-neutral economy. 1-4 Over the past decade, a number of synthetic catalysts that mediate electrochemical HER have emerged to advance this endeavor. 5-7 Cobalt polypyridyl complexes stand out as effective earth-abundant HER catalysts owing to their synthetic tunability and ability to stabilize key intermediates.^{8,9} In particular, the strong field Nbased ligands are capable of supporting low-valent cobalt centers and hydride intermediates required to shuttle electrons and protons during catalysis. After Chang and co-workers developed a cobalt-based HER catalyst supported by the tetradentate ligand 2-bis(2-pyridyl)(methoxy)methyl-6-pyridylpyridine (PY4) (Scheme 1a),10 much effort has been directed toward optimizing the performance of this class of catalysts by systematically varying the ligand design. $^{11-19}$ This includes varying the donor ability of the ligand substituents, changing ligand denticity, and incorporating redox active sites and pendant basic moieties.

The highly modular nature of homogeneous catalysts allows for the exploration of mechanisms by which HER is mediated and identification of how the ligand structure and electronic properties impact the operative mechanisms. In this context, ligand acid—base functionality has been heavily explored to improve kinetics of proton transfer in forming metal hydride intermediates. For instance, Nocera and co-workers developed cobalt "hangman" porphyrin complexes (Scheme 1b), where they demonstrated that installation of acid—base functional groups in close proximity to the metal center enhances the rate constant for proton transfer to the metal centers, leading to faster HER catalysis. ^{20,21} Conversely, proton transfer kinetics involving metal hydride complexes is known to be slow in the absence of a kinetically accessible basic site. ²² The sluggish kinetics has been attributed to the large structural and electronic changes associated with direct metal pronation. In the study of a cobalt polypyridyl catalyst [Co(bapbpy)Cl]⁺ (bapbpy = 6,6'-bis(2-aminopyridyl)-2,2'-bipyridine) bearing

Received: September 20, 2023 Revised: January 17, 2024 Accepted: January 18, 2024 Published: February 5, 2024





Scheme 1. Molecular Structure of Referenced Cobalt-Based HER Catalysts

pendant amine groups (Scheme 1c), varying the acid strength and applied potential enables access to different HER mechanisms involving protonation at the pendant basic sites. However, direct protonation at the reduced Co(I) center to generate a Co(III) hydride intermediate was not accessible. DFT calculations indicate that the bapbpy ligand is highly flexible, which suggests a large intrinsic barrier to directly protonate the metal center. Although these efforts demonstrate unique mechanistic pathways for HER facilitated by pendant bases, the hypothesis that structural and electronic properties of the ligand dictate the protonation site has been largely untested. Studies of a cobalt polypyridyl catalyst with a pendant base supported by a ligand with limited structural and electronic changes may facilitate the efficient formation of metal hydride intermediates through direct metal protonation.

Although cobalt polypyridyl catalysts have shown promise for mediating HER, little is understood about their reaction pathways. This makes it difficult to extract kinetic information or map thermochemical properties of the catalytic intermediates. This challenge is in part due to the complexity of the catalytic cycle, especially when ligand protonation sites are involved. Additionally, kinetic information is generally dependent on the catalytic mechanism and can vary dramatically under different reaction conditions. Therefore, it is essential to have a deep understanding of the mechanism to correctly quantify and interpret kinetic and thermodynamic data. A notable example is the HER catalyst [Ni(P2PhN2Ph)- $(CH_3CN)^{2+}$ $(P_2^{Ph}N_2^{Ph} = 1,3,5,7-\text{tetraphenyl-1,5-diaza-3,7-}$ diphosphacyclooctane) that exhibits two distinct mechanisms depending on the strength and concentration of the proton 4 Consequently, different kinetic analyses were carefully chosen to determine rate constants for the elementary steps associated with each mechanism. The determination of these parameters has directly informed the design of improved catalysts by providing a thorough understanding of how to control electron and proton mobility during catalysis.

Hamann and co-workers recently reported a series of cobalt complexes supported by polypyridyl ligands bearing a pendant pyridyl base and their applications as redox shuttles in dyesensitized solar cells ([Co^{II}py]²⁺ and substituted derivatives (Scheme 1d).²⁵ Interestingly, these [Co^{II}py]²⁺ complexes

undergo a reversible structural rearrangement from five-coordinate Co(II) to six-coordinate Co(III) complexes, wherein the pendant pyridine is coordinated to the cobalt center. Despite the intramolecular rearrangement, the strong-field polypyridyl ligands promote a low-spin Co(II) configuration, which reduces the inner-sphere reorganization energy in the Co(III/II) electron transfer process. The structural rigidity and limited electronic changes caused by the strong-field multidentate ligands, combined with the pendant pyridyl base, present an opportunity to explore unique reactivity pathways achievable through this molecular system.

Herein, we describe for the first time the ability of [Co^{II}py]²⁺ to mediate electrochemical HER. Structural analyses, as well as electrochemical measurements, indicate minimal structural and electronic changes upon reduction of [Co^{II}py]²⁺ by one electron. Reactivity studies of the isolated Co(I) species with a series of organic acids reveal that a Co(III) hydride species is involved as a viable intermediate for HER. The mechanisms underlying electrocatalytic HER were unraveled across a range of acid strengths. Rate constants for the elementary steps were quantified using a combination of electrochemical analysis and digital simulations. These results support the formation of the Co(III) hydride intermediate through direct metal protonation. Proton transfer to the pendant pyridyl base occurs after the Co(III) hydride intermediate is further reduced and/or when the acid used is sufficiently strong. The detailed understanding of the mechanisms enables the determination of thermodynamic and kinetic parameters associated with key intermediates in the proposed electrocatalytic HER mechanisms.

■ RESULTS AND DISCUSSION

Electrochemical Properties of [Collpy]²⁺. Cyclic voltammograms of $[Co^{II}py]^{2+}$ in acetonitrile exhibit two electrochemically reversible one-electron waves at $E_{1/2} = -0.21$ and -1.12 V (all values reported vs Fc^{+/0} couple) corresponding to the Co(III/II) and Co(II/I) reductions, respectively (Figure 1). The observed reduction potentials are consistent with previously reported values measured under similar conditions.²⁵ Scan rate dependence of the peak current yielded diffusion coefficients of $D = 2.8 \times 10^{-6}$ and 4.3×10^{-6} cm² s⁻¹ associated with the Co(III/II) and Co(II/I) couples, respectively (see the Supporting Information). The diffusion coefficients are within the same order of magnitude as those reported for other cobalt complexes despite the difference in overall charges and sizes. ^{20,26,27} The heterogeneous electron transfer rate constants $(k_s s)$ were determined using a trumpet plot analysis and simulated working curves (see the SI for more details). k_s values of 0.024 and 0.17 cm s⁻¹ were quantified for the Co(III/II) and Co(II/I) couples, respectively. The value of k_s for the Co(III/II) reduction couple is slightly lower than that reported for a cobaloxime derivative, Co- $(dmgBF_2)_2(CH_3CN)_2$ $(dmgBF_2$ = difluoroboryl-dimethylglyoxime) $(k_s = 0.054 \text{ cm s}^{-1})^{28}$ Reduction of Co(III) to Co(II) generally proceeds with slow electron-transfer kinetics due to a low-spin to high-spin transition of the ground-state electron configuration. ^{27,28} However, the Evans method measurement of $[\mathbf{Co^{II}py}]^{2+}$ gives a magnetic moment of μ_{eff} = 1.8 $\mu_{\rm B}$, consistent with a low-spin d^7 configuration. Therefore, the relatively slow electron-transfer kinetics may not primarily involve significant electronic changes. Instead, the low k_s value may be attributed to the previously observed intramolecular rearrangement of the pendant pyridine, which

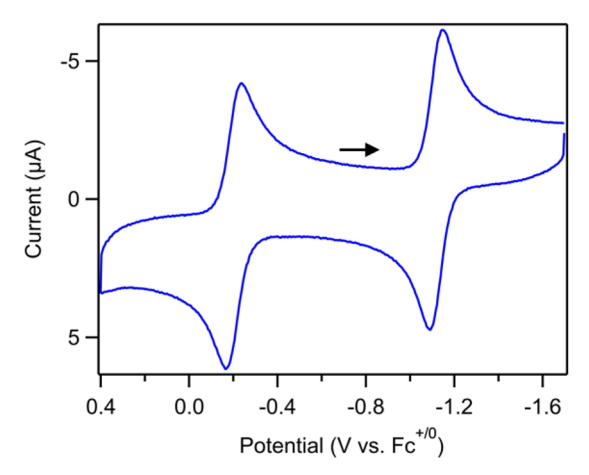


Figure 1. Cyclic voltammogram of 0.2 mM [CoPY5Im][BArF₂₄]₂ ([Co^{II}py]²⁺) in CH₃CN with 0.25 M [Bu₄N][PF₆] as a supporting electrolyte recorded at 200 mV/s scan rate. $E_{1/2}(\text{Co}^{\text{III/II}}) = -0.21 \text{ V vs Fc}^{+/0}$ and $E_{1/2}(\text{Co}^{\text{III/I}}) = -1.12 \text{ V vs Fc}^{+/0}$. All voltammograms were recorded under a N₂ atmosphere with a 3 mm diameter glassy carbon working electrode, a 3 mm diameter glassy carbon counter electrode, and a Ag/AgNO₃ reference electrode. All voltammograms were referenced to Fc^{+/0} using a ferrocene internal reference. Applied voltage was corrected for ohmic drop using positive feedback $R_{\rm u}$. All voltammograms are plotted in polarographic convention; arrow shows starting point and direction of scan.

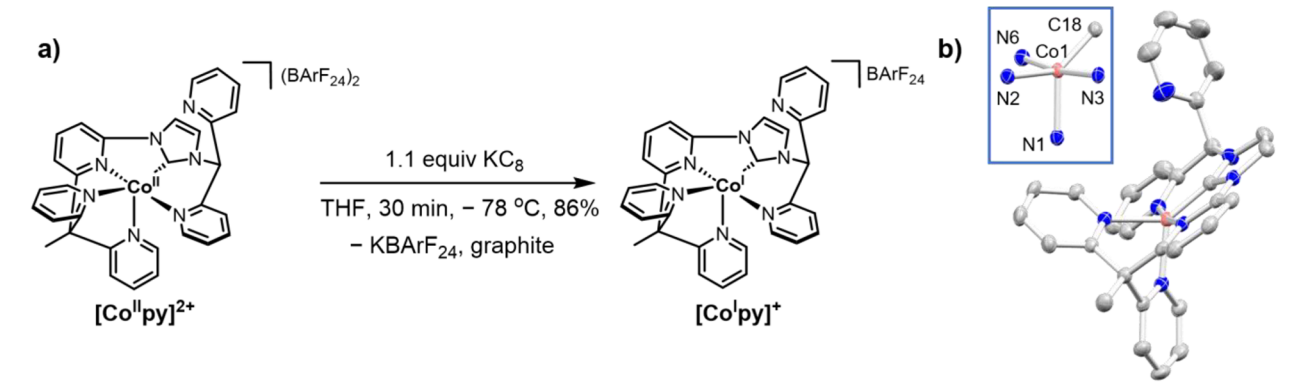
coordinates to the cobalt center in the Co(III) oxidation state but not in the Co(II) oxidation state. Nevertheless, the fast electron-transfer kinetics of the Co(II/I) couple suggests that there are fewer electronic and structural changes upon reduction compared to the Co(III/II) reduction. This encouraged us to isolate and study the reduced Co(I) species in the context of metal hydride formation.

Isolation of Reactive Co(I) Intermediate and Structural Analysis. The relatively fast electron-transfer kinetics of the Co(II/I) couple and its mild reduction potential suggest a facile chemical reduction of $[\mathbf{Co^{II}py}]^{2+}$. Indeed, the reaction of $[\mathbf{Co^{II}py}]^{2+}$ with 1.1 equiv of KC_8 in THF at -78 °C afforded $[\mathbf{Co^{I}py}]^{+}$ in 86% yield after 30 min (Scheme 2a). The ¹H NMR spectrum of $[\mathbf{Co^{I}py}]^{+}$ is well-resolved, which is consistent with a low-spin d^8 configuration (Figure S45). Analysis of the ¹H NMR spectrum reveals that $[\mathbf{Co^{I}py}]^{+}$ is C_1 symmetric, in agreement with the solid-state molecular

structure as determined by single-crystal X-ray diffraction (Scheme 2b). The Co-N bond lengths span the range of 1.889(3)-2.032(3) Å, whereas the Co-C bond is shorter (1.764(4) Å) because of the strong covalent bond between Co and the strongly σ -donating N-heterocyclic carbene ligand. Notably, the Co-N and Co-C bond lengths increase systematically with the oxidation state of the cobalt, indicating that the covalent bonds become weaker upon removing electrons from the cobalt center (Table S2). Although the oxidation of [Co^{II}py]²⁺ furnishes a six-coordinate complex, [Co^{III}py]³⁺, because of the intramolecular rearrangement,² the pendant pyridine remains unbound in the five-coordinate [Co^Ipy]⁺ complex. Further analysis of the bond angles around the cobalt center gives a geometric index of $\tau = 0.55$, indicating that the geometry of [Co^Ipy]⁺ is in between square pyramidal and trigonal bipyramidal ($\tau = 0$ and $\tau = 1$ describe ideal square pyramidal and trigonal bipyramidal geometries, respectively) (Scheme 2b, inset).²⁹ The slightly lower geometric index of $[\mathbf{Co^{II}py}]^{2+}$ ($\tau = 0.28$) is consistent with the geometry of the complex being closer to square pyramidal than [Co^Ipy]⁺ is (see SI for more details regarding geometry index analyses of [Co^Ipy]⁺ and [Co^{II}py]²⁺). The structure of [Co^Ipy]⁺ is slightly distorted from square pyramidal; this can be attributed to the geometric strain created by the contraction of bonds around the cobalt center. The multidentate ligand therefore "preorganizes" [Colpy]+ such that less structural and electronic changes are expected when forming a six-coordinate metal hydride complex. This is in contrast to the more commonly observed transition from trigonal bipyramidal to octahedral geometry in geometrically flexible reduced metal complexes.²²

Stoichiometric Reactions of $[Co^lpy]^+$ and $[Co^lpy]^{2+}$ with Organic Acids. The prediction of minimal electronic and structural rearrangement of $[Co^lpy]^+$ upon protonation prompted an investigation into the reactivity of $[Co^lpy]^+$ with a series of organic acids with pK_a values spanning the range of 9.43–25.44 in acetonitrile. Addition of 10 equiv of 4-bromoanilinium $(pK_a = 9.43)^{30}$ and 4-methoxypyridinium $(pK_a = 14.23)$ to solutions of $[Co^lpy]^+$ in CD_3CN resulted in a very rapid color change from purple to yellow and gas evolution. The 1H NMR spectra of the reaction mixtures after 1 h show that $[Co^{ll}py]^{2+}$ is formed as the primary reaction product (Figure S4). Headspace analysis of the reaction between $[Co^lpy]^+$ and 4-methoxypyridinium by gas chromatography identified H_2 as the primary gaseous component. The

Scheme 2. Synthesis of [Co^Ipy]⁺ and Its Solid-State Molecular Structure^a



"Solvents, hydrogen atoms, and tetrakis(3,5-bis(trifluoromethyl)phenyl)borate anion (BArF₂₄") of the solid-state molecular structure are omitted for clarity. Thermal ellipsoids are shown at 50% probability. Inset: truncated structure showing the coordination geometry around the cobalt center.

observed yield is consistent with a 1:0.38 ratio of $[\mathbf{Co^Ipy}]^+$ to \mathbf{H}_2 . This stoichiometry and the formation of $[\mathbf{Co^{II}py}]^{2+}$ suggest a metal hydride species (i.e., $[\mathbf{Co^{II}(H)py}]^{2+}$) as a reactive intermediate in a homolytic HER mechanism. In the homolytic pathway, a bimolecular reaction involving two $[\mathbf{Co^{II}(H)py}]^{2+}$ results in the \mathbf{H}_2 evolution and formation of $[\mathbf{Co^{II}py}]^{2+}$. The rationale for this mechanistic consideration is explained in greater detail in the SI. Whereas $[\mathbf{Co^{III}(H)py}]^{2+}$ undergoes a biomolecular reaction in this stoichiometric reactivity, different pathways may be operative under electrochemical conditions, whereby $[\mathbf{Co^{III}(H)py}]^{2+}$ can be further reduced.

Treatment of [Co^Ipy]⁺ with 10 equiv of 4-dimethylaminopyridinium (p $K_a = 17.95$) and benzoic acid (p $K_a = 21.51$) also yielded H₂ and [Co^{II}py]²⁺ but at a significantly slower rate (full conversion of [Co^Ipy]⁺ was observed after 3 h by ¹H NMR spectroscopy, Figure S5). In addition to proton resonances corresponding to H_2 and $[Co^{II}py]^{2+}$, a new set of peaks slowly grew and disappeared over 24 h. Although attempts to isolate or characterize this species have not been successful, this species is likely not $[Co^{III}(H)py]^{2+}$ due to the absence of the characteristic negative ¹H NMR chemical shifts associated with hydride species. Because of this side reaction observed at longer reaction time, the electrocatalytic experiments were limited to acids with p K_a < 17.95 (vide infra). No reaction was observed between [Co^Ipy]⁺ and 4-chlorophenol $(pK_a = 25.44)$, which is the weakest acid explored in this study. Together, these stochiometric experiments suggest that [Co^Ipy]⁺ is competent in proton reduction in the absence of additional reductant and that $[Co^{III}(H)py]^{2+}$ likely formed in these reactions as a viable intermediate. These observations also provide an estimate for a pK_a value of $[Co^{III}(H)py]^{2+}$, bracketed to be between 21.51 and 25.44 in acetonitrile, which is comparable to those observed for a family of [Co^{III}(H)Cp- $(dxpe)(CH_3CN)]^{2+}$ complexes (dxpe = 1,2-bis(di(aryl/alkyl)phosphino)ethane).26,31

The reactivity of $[\mathbf{Co^{II}py}]^{2+}$ with organic acids (5.06 < p K_a < 11.86) in acetonitrile was also investigated to map out the acid-base properties of the molecular system. Treatment of $[\mathbf{Co^{II}py}]^{2+}$ with either 1 equiv of 2,6-dichloroanilinium (p K_a = 5.06) or 1 equiv of 4-bromoanilinium (p $K_a = 9.43$) resulted in a partial protonation to form the ligand protonated species, $[Co^{II}py(H)]^{3+}$, which can be reversibly deprotonated with 4methoxypyridine (Figure S6). No reaction was observed when $[\mathbf{Co^{II}py}]^{2+}$ was treated with 4-methoxyanilinium $(\mathbf{p}K_{a} =$ 11.86). Given the reversible protonation behavior, the p K_a value of $[Co^{II}py(H)]^{3+}$ was quantified via spectrophotometric titration with 4-bromoanilinium and 4-cyanoanilinium (pK_a = 7) (Figure S7). A p K_a value of 6.8 was determined, about half of that of free pyridinium (p $K_a = 12.53$), which suggests a strong electronic influence of the cobalt center and the rest of the ligand on the pendant pyridine.

Electrocatalytic HER Reactivity of [Co^{II}py]²⁺. Given the accessibility to the proposed hydride intermediate and the presence of the pendant pyridine ligand, we were interested in exploring the electrocatalytic HER reactivity mediated by this molecular system. We investigated the catalytic responses across a wide range of acids and discovered that the voltammetric responses varied tremendously. This finding prompted us to realize that, to analyze the reactivity and quantify catalysis, we needed to understand how proton-coupled electron transfer processes manifest in voltammetric responses and how the reaction pathway is dictated by acid

strength. Below, we discuss our methodology for deciphering the operative mechanism(s) and quantifying catalytic activity as a function of acid strength. Specifically, we will extract mechanistic information from cyclic voltammograms of catalyst $[\mathbf{Co^{II}py}]^{2+}$ recorded with low acid concentrations (0-2 equiv). With the detailed mechanistic understanding, we will then discuss kinetic analyses for proton transfer reactions. Next, cyclic voltammograms of catalyst $[\mathbf{Co^{II}py}]^{2+}$ with high acid concentrations will be analyzed to further identify the operative mechanisms and quantify catalytic activity. Finally, digital simulations are used to support the proposed mechanisms and estimate rate constants for proton transfer that could not be measured experimentally.

Electrocatalytic HER in the Weak Acid Regime. To probe the ability of $[\mathbf{Co^{II}py}]^{2+}$ to mediate the electrochemical reduction of protons to hydrogen, the voltammetric responses of $[\mathbf{Co^{II}py}]^{2+}$ were recorded in the presence of organic acids $(14.23 < pK_a < 14.47)$. In this acid regime, $[\mathbf{Co^{II}py}]^{2+}$ is not protonated prior to the electrochemical measurements because its conjugate acid, $[\mathbf{Co^{II}py(H)}]^{3+}$, is a stronger acid with a pK_a value of 6.8 (*vide supra*). At low acid concentrations (0.2-0.4 mM), the Co(II/I) couple becomes chemically irreversible, and a new chemically irreversible wave $(E_{pc} = -1.39 \text{ V})$ is observed in the voltammogram (Figure 2a and Figure S8). Although both waves gain reversibility with increasing scan

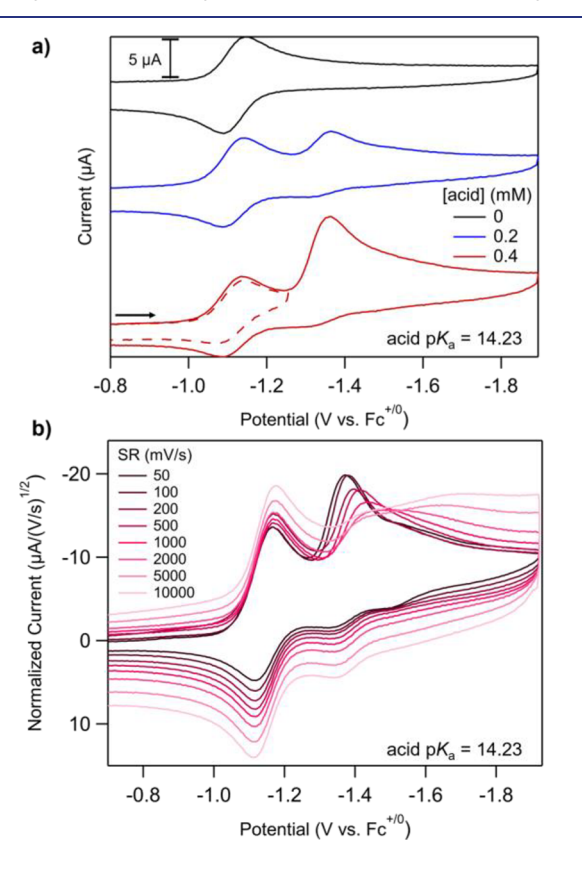


Figure 2. (a) Cyclic voltammograms of 0.2 mM $[Co^{II}py]^{2+}$ in CH₃CN with no acid (black) and with additions of 0.2 mM (blue) and 0.4 mM (red) 4-methoxypyridinium $(pK_a = 14.23)$. The dashed red trace is the voltammogram of 0.2 mM $[Co^{II}py]^{2+}$ in CH₃CN with 0.4 mM (red) 4-methoxypyridinium with a switching potential of -1.25 V. Voltammograms recorded at 200 mV/s in 0.25 M $[NBu_4][PF_6]$. (b) Cyclic voltammograms of 0.2 mM $[Co^{II}py]^{2+}$ in CH₃CN with 0.2 mM 4-methoxypyridinium recorded at various scan rates in 0.25 M $[NBu_4][PF_6]$.

Table 1. Rate Constants Associated with Chemical Reactions with Organic Acids

acid regime	acid identity	${\rm acid} \ pK_{\rm a} \ ({\rm CH_3CN})^{30}$	$(M^{-1} s^{-1})^a$	$(M^{-1} s^{-1})^b$	$k_{\text{PT3}} \text{ for } C_3 \ (M^{-1} \text{ s}^{-1})$	$k_{\Omega} \operatorname{for} \operatorname{C}_{\operatorname{H2}} (\operatorname{s}^{-1})^{c}$	$\frac{k_{\gamma} \text{ for } C_{H_{2}^{2}}}{(M^{-1} \text{ s}^{-1})^{2}}$
weak	2-aminopyridinium	14.47	6.3×10^3	8.2×10^4		4.5×10^{2}	
weak	4-methoxypyridinium	14.23	1.4×10^4	3.1×10^4		4.5×10^{2}	
intermediate	2-methylpyridinium	13.32	1.6×10^{5}	1.6×10^{6d}		4.5×10^{2}	
intermediate	pyridinium	12.53	3.4×10^{6}	3.4×10^{7d}		4.5×10^{2}	
intermediate	4-methoxyanilinium	11.86	8.1×10^{6}	8.1×10^{7d}		4.5×10^{2}	
intermediate	anilinium	10.62	4.3×10^7	4.3×10^{8d}		4.5×10^{2}	
strong	2,6-dichloroanilinium	5.06	1×10^{10e}	1×10^{10e}	$1 \times 10^{10^f}$	4.5×10^{2}	$\sim 10^{5g}$

^aQuantified from peak shift analysis using eq 1. ^bDetermined from plateau current analysis and eq 2 unless otherwise noted. ^cEstimated from an average limiting current value $(i_{c,max})$ of 120 μ A and eq 3. ^dArbitrarily set to be an order of magnitude higher than k_{PT1} for simulation purposes. ^cEstimated from the LFER plot to reach diffusion limit. ^fSet to reach diffusion limit to rapidly establish equilibrium for ligand protonation. ^gObtained from digital simulations.

rate, the magnitude of the current of the second wave decreases with higher scan rates (Figure 2b and Figure S9). These voltammetric responses suggest an ECEC type mechanism in which the fast electron transfer (E_1) associated with the Co(II/I) reduction is followed by an irreversible chemical reaction with acid (C₁) to generate a new chemical species. Assignment of the first E_1C_1 step is further supported by the shift of the Co(II/I) peak position as a function of scan rate and acid concentration for all acids used, as expected for an EC reaction under kinetic control (Figures S20 and S21). The chemical species formed by the initial E_1C_1 reaction then undergoes a reduction (E2). This reduction step is evidenced by the new voltammetric wave observed with $E_{pc} = -1.39 \text{ V}$. The lack of chemical reversibility of this second wave indicates that the reduced species generated through this $E_1C_1E_2$ process is further reactive with protons (C_2) .

The observation that the waves at -1.12 and -1.39 V regain reversibility upon increasing scan rate indicates that the chemical steps C₁ and C₂ are relatively slow. The reduction of current in the second wave at faster scan rates can be explained by the fact that less of the new chemical species is generated from the first chemical step (C_1) as scan rate is increased. Note that pyridinium and anilinium acids are directly reduced by the electrode at the potentials slightly more negative than those of the second wave (-1.2 to -2.0 V), 32 and current increases associated with these direct acid reductions were observed at fast scan rates (Figure 2b and Figures S13-S19). This observation supports our hypothesis that the chemical steps involving protons are relatively slow. At fast scan rates, there is less time for the reaction between the cobalt species and acid, thus affording more direct acid reduction. Based on these collective observations made using 0-2 equiv of acid, we propose that the electron transfer step (E_1) generates $[Co^lpy]^+$ and the subsequent chemical step (C_1) is likely the protonation of [Co^Ipy]⁺. Subsequent electrochemical and chemical reactions (E2C2) of the chemical species generated from this E₁C₁ process will be discussed later.

To probe the protonation site involved with chemical step C_1 , switching potential experiments were employed. The formation of metal hydride species can occur through two major pathways: (1) direct protonation of the metal center or (2) protonation of the pendant base followed by tautomerization. To distinguish between the two possible pathways under electrochemical conditions, cyclic voltammograms were recorded for $[\mathbf{Co^{II}py}]^{2+}$ in the presence of 2 equiv of 4-methoxypyridinium with a switching potential of -1.25 V (Figure 2a). At this switching potential, the scan direction is

reversed, and the electrochemically formed species should undergo an oxidation via a proton-coupled electron transfer (PCET) reaction to regenerate [Co^{II}py]²⁺. In this experiment, the Co(II/I) couple remained irreversible at 200 mV/s, which indicates a kinetically slow PCET oxidation on the electrochemical time scale. It is important to note that upon increasing scan rates, this reduction wave regains chemical reversibility, and this behavior is attributed to the inherently slow C₁ step (Figure S10). PCET processes involving ligandbased deprotonation are generally fast, and they have been previously observed to exhibit electrochemically reversible redox couples. 33,34 In these studies, the fast ligand-based PCET events have been attributed to the smaller intrinsic barriers compared to those related to metal-based PCET processes. The relatively slow PCET reaction observed in this study suggests that the proton transfer reaction likely involves (de)protonation at the cobalt center. Rapid protonation at the pendant pyridine followed by a slow intramolecular proton transfer to the cobalt center is also a possible explanation, but the switching potential experiments alone could not distinguish between the two mechanisms.

To further probe the operative mechanism for the C_1 process, which as described above is under kinetic control, the proton transfer rate constant associated with the chemical step $(k_{\rm PT1})$ was determined by monitoring the shift of the peak potential of the Co(II/I) couple $(E_{\rm pc})$ with acid concentration and scan rate (ν) using eq 1:³⁵

$$E_{\rm pc} = E_{1/2} - \frac{RT}{F} (0.78) + \frac{RT}{2F} \ln \frac{k_{\rm PT1} [\rm H^+] RT}{F \nu}$$
 (1)

where R, T, and F are the gas constant, temperature, and the Faraday constant, respectively, and $E_{1/2}$ is the potential of the one-electron reversible electrochemical event in the absence of acid. The E_{pc} was found to shift to more positive potentials with increasing acid concentration and to more negative potentials with increasing scan rate, with the characteristic slope of ~30 mV dec⁻¹ for an EC reaction (Figures S20 and $(821)^{.35}$ A rate constant of $k_{PT1} = 1.4 \times 10^4 \text{ M}^{-1} \text{ s}^{-1}$ is quantified for the proton donor 4-methoxypyridinium (pK_a = 14.23) and $k_{\rm PT1} = 6.3 \times 10^3 \ {\rm M}^{-1} \ {\rm s}^{-1}$ for 2-aminopyridinium $(pK_a = 14.47)$. These measurements were also performed using acids spanning over 4 p K_a units (k_{PT1} ranging from 6.3×10^3 to $4.3 \times 10^7 \,\mathrm{M}^{-1} \,\mathrm{s}^{-1}$), although the results for stronger acids will be discussed in the subsequent section. All kinetic information associated with the chemical reactions proposed in the catalytic cycles are recorded in Table 1. Across 4 p K_a units, a linear free energy relationship (LFER) is observed between $log(k_{PT1})$ and

the p K_a of the acids with a slope of -1.0 (Figure 3). The rate constant increases as the acid p K_a is lowered, in agreement

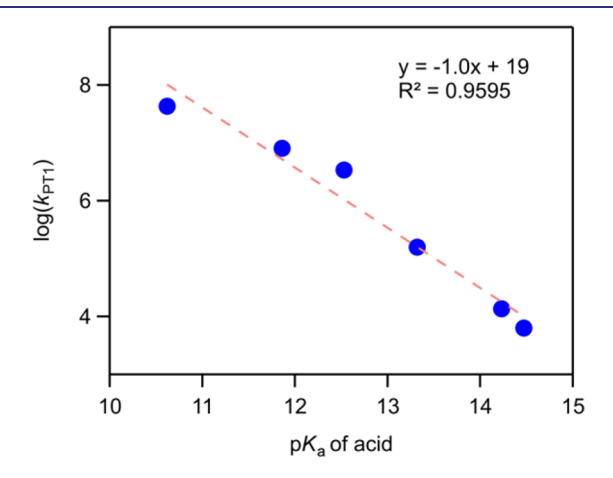


Figure 3. Logarithm of rate constants for the protonation of $[Co^{I}py]^{+}(k_{PT1})$ as a function of acid pK_a in CH₃CN.

with the previously observed trends for the formation of cobalt hydride complexes. 26,28,31 The p $K_{\rm a}$ -dependent trend suggests a common mechanism for the protonation of $[{\bf Co^Ipy}]^+$ for all acids used for this analysis regardless of their p $K_{\rm a}$ values.

The LFER analysis reveals the effect of structural and electronic changes on proton transfer kinetics and operative mechanisms. The LFER slope of -1.0 is comparable to that observed for the formation of a putative Co(III) hydride in the study of the cobaloxime $Co(dmgBF_2)_2(CH_3CN)_2$ (slope = -0.97).²⁸ However, the k_{PT1} values for protonating [Co¹py]⁺ fall below the k_{PT} values observed for the cobaloxime system at similar driving forces, as demonstrated in the Brønsted plot (Figure S47). The higher kinetic barrier to protonate [Colpy]+ may be attributed to the greater geometric rearrangement during the proton transfer process. Specifically, [Co^Ipy]⁺ undergoes a transition from an intermediate structure between square pyramidal and trigonal bipyramidal ($\tau = 0.55$) to an octahedral configuration. Conversely, cobaloxime transitions from an almost ideal square pyramidal geometry ($\tau = 0.03$, calculated from the solid-state molecular structure of [Co^I(dmgBF₂)₂py]⁻)³⁶ to octahedral upon protonation. As noted above, the reduction of current for the E2 step at fast scan rates indicates that C_1 is slow. Consistently, the proton transfer rate constants found here are comparatively low across all acids studied, lending support for direct metal protonation of [Co^Ipy]⁺ to form [Co^{III}(H)py]²⁺ (Scheme 3). The significantly slower proton transfer kinetics compared to [Co^ICp(depe)]⁺ (depe = 1,2-bis(diethylphosphino)ethane), where protonation occurs at the Cp ligand prior to the

formation of the Co(III) hydride species,³¹ further supports the direct metal protonation mechanism (Figure S47).

At high acid concentrations (2–18 mM for 4-methoxypyridinium and 2–20 mM for 2-aminopyridinium), an increase in cathodic current and a loss of reversibility were observed at the second wave, indicating catalytic acid reduction (Figures 4).

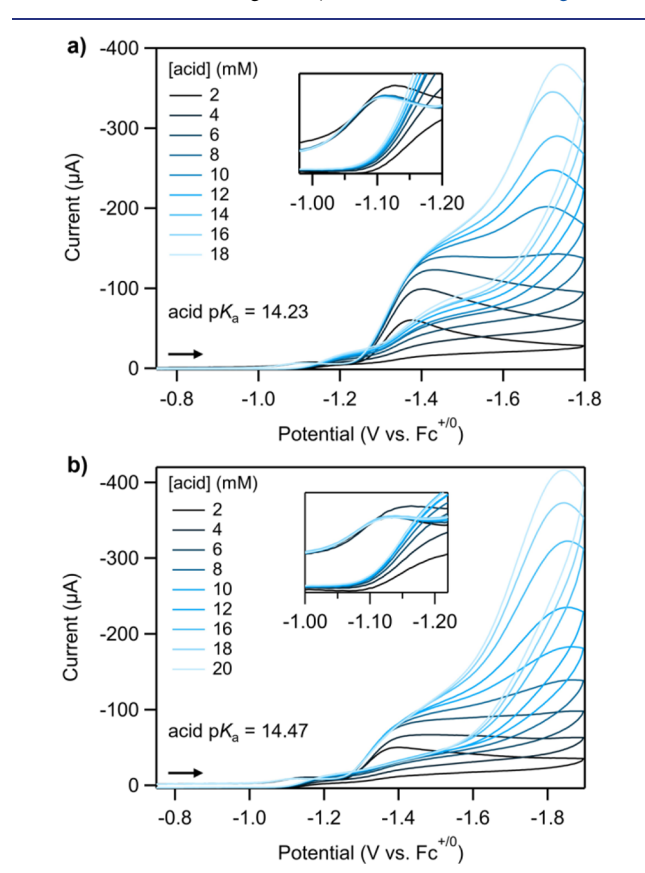


Figure 4. (a) Cyclic voltammograms of 0.2 mM $[Co^{II}py]^{2+}$ in CH₃CN with additions of 2–18 mM 4-methoxypyridinium. (b) Cyclic voltammograms of 0.2 mM $[Co^{II}py]^{2+}$ in CH₃CN with additions of 2–20 mM 2-aminopyridinium. Voltammograms recorded at 200 mV/s in 0.25 M $[NBu_4][PF_6]$. Insets: shifts of Co(II/I) reduction couple as a function of acid concentration.

Controlled potential electrolysis (CPE) performed using 100 mM 4-methoxypyridinium at -1.48~V vs $Fc^{+/0}$ and a reticulated vitreous carbon electrode yielded a Faradaic efficiency of 85% accounting for H_2 in both the headspace and solution (quantified by gas chromatography). The applied potential was set to be at E_2 to access the reduction of $[\textbf{Co}^{III}(\textbf{H})\textbf{py}]^{2+}$. This ensures that the charge passed is primarily a result of the $E_1C_1E_2C_2$ pathway, not the

Scheme 3. Proposed E₁C₁ Step for the Formation of [Co^{III}(H)py]²⁺

bimolecular reaction of $[\mathbf{Co^{III}(H)py}]^{2+}$, as observed in the stochiometric reactivity of $[\mathbf{Co^{II}py}]^+$ with acids (*vide supra*). To calculate a catalytic turnover frequency that accounts for the amount of the catalyst within the reaction—diffusion layer, a 3 mm glassy carbon disc electrode was used in a separate unstirred CPE experiment. This electrocatalysis corresponds to an overpotential (η) of 690 mV with a turnover frequency (TOF) of $2.7 \times 10^2 \, \mathrm{s^{-1}}$ (see the SI for more details regarding CPE experiments). These experiments confirm that our catalyst $[\mathbf{Co^{II}py}]^+$ is selective for proton reduction to H_2 . Note that trace crossing on the anodic sweep was observed at high acid concentrations and slow scan rates (Figure 4 and Figures S26 and S27). This effect will be rationalized below through the use of digital simulations.

The catalytic waves approach a plateau shape with increasing acid concentration (>2 mM), and the plateau currents become scan rate independent (Figures S26 and S27). Notably, as acid concentrations exceed 6 mM, the current response becomes independent of acid concentration, reaching a limiting current value $(i_{c,max})$ of ca. 140 μ A for 4-methoxypyridinium (Figure 4a) and 100 μ A for 2-aminoanilinium (Figure 4b). An acidindependent behavior at high concentrations of strong acids has been previously observed for Co(dmgBF₂)₂(CH₃CN)₂. In this cobaloxime study, the current response reaches a limiting value that is constant across all acids, and the concentration of acid required to achieve the limiting current value decreases as acid strength increases. The authors hypothesized that this acid-independent behavior corresponds to the rate-limiting H-H bond formation or release of H₂ from a doubly protonated cobalt species formed in an ECEC mechanism. Here, the catalytic plateau current using [Co^{II}py]²⁺ is reached at a similar concentration for both acids (ca. 8 mM) due to their similarity in acid strength. However, it should be noted that both acids exhibit direct proton reduction at potentials overlapping with the catalytic peaks, which could affect the slight deviation in the observed limiting currents. Therefore, we propose a similar ECEC mechanistic scenario; the first E_1C_1 step forms $[Co^{III}(H)py]^{2+}$, which is further reduced and protonated in the subsequent E_2C_2 step to generate doubly protonated species $[Co^{II}(H)py-$ (H)]²⁺ (Scheme 4). Release of H_2 (C_{H2}) is rate limiting at high acid concentrations. A related study using a cobalt complex bearing pendant amines, [Co(bapbpy)Cl]⁺, as an HER catalyst also revealed a ligand-protonated Co(II) hydride species as a key intermediate.

Despite the acid-independent behavior observed at high acid concentrations (>6 mM), we were able to determine the

Scheme 4. Proposed ECEC Mechanism to Release H₂ in the Weak Acid Regime

$$[Co^{II}(H)py(H)]^{2+}$$

$$[Co^{II}(H)py(H)]^{2+}$$

$$[Co^{II}(H)py]^{+}$$

$$[Co^{II}(H)py]^{+}$$

$$[Co^{III}(H)py]^{2+}$$

proton transfer rate constant to form $[\mathbf{Co^{II}(H)py(H)}]^{2+}(k_{PT2})$ by analyzing the plateau current (i_c) as a function of acid concentration $(C_A^0 = 2-6 \text{ mM})$ in eq 2:³⁷

$$i_c = 2FAC_p^0 \sqrt{D} \frac{1}{\frac{1}{\sqrt{k_{PT1}C_A^0}} + \frac{1}{\sqrt{k_{PT2}C_A^0}}}$$
(2)

where A, C_p^0 , and D are the electrode surface area, bulk concentration of the catalyst, and diffusion coefficient determined from the scan-rate dependence study, respectively. Note that this equation applies to an ECEC mechanism in which the electron transfer events occur at the electrode and the first reduction potential is more positive than the second reduction potential. By using the $k_{\rm PT1}$ values quantified from the peak-shift analysis, $k_{\rm PT2}$ values of 3.1×10^4 and 8.2×10^4 M⁻¹ s⁻¹ were obtained to describe the kinetics for the formation of $[{\bf Co^{II}(H)py(H)}]^{2+}$ using 4-methoxypyridinium and 2-aminopyridinium, respectively (see the SI for more details). The values of $k_{\rm PT2}$ are slightly higher than those of $k_{\rm PT1}$ for both acids, which are consistent with a less kinetically demanding ligand-based protonation in forming $[{\bf Co^{II}(H)py-(H)}]^{2+}$.

Although the catalytic wave partially overlaps with the direct acid reduction, a first-order rate constant describing the acid-independent step (k_{Ω}) was estimated by using the average value for $i_{\rm c,max}$ for the two acids (120 μ A) and eq 3:³⁷

$$i_{c,\text{max}} = 2FAC_P^0 \sqrt{Dk_{\Omega}}$$
(3)

where A, C_p^0 , and D are the electrode surface area, bulk concentration of the catalyst, and diffusion coefficient determined from the scan-rate dependence study in the absence of proton source, respectively. A rate constant of ca. $4.5 \times 10^2 \, \mathrm{s^{-1}}$ was quantified. As noted above, this rate constant likely describes the rate-limiting H–H bond formation or H_2 release that is acid-concentration- and p K_a -independent. This value is more of an estimate because $i_{c,max}$ is likely convoluted by the current of the direct acid reduction. However, it is within the same order of magnitude with the TOF determined from the CPE experiment (TOF = $2.7 \times 10^2 \, \mathrm{s^{-1}}$), suggesting that this rate constant describes the overall kinetics of this catalysis.

Because the catalytic wave is convoluted by the current resulting from direct acid reduction at high acid concentrations, digital simulations were used to support the proposed E₁C₁E₂C₂ pathway followed by a rate-limiting H-H bond formation or H2 release under the low acid concentration regime (0.2–0.4 mM). Gratifyingly, the voltammograms were reproduced across all scan rates by using the pK_a values of 23.5 and 16.4 estimated for $[Co^{III}(H)py]^{2+}$ and $[Co^{II}(H)py(H)]^{2+}$, respectively. The p K_a value of $[Co^{III}(H)py]^{2+}$ is taken as the average of the estimated p K_a range (21.51 to 25.44), and that of $[Co^{II}(H)py(H)]^{2+}$ is estimated using digital simulations (Figure S28). The $k_{\rm PT1}$, $k_{\rm PT2}$, and k_{Ω} values of 1.4×10^4 , 3.1×10^4 , and $4.5 \times 10^2 \ {\rm s}^{-1}$, respectively, experimentally quantified for 4-methoxypyridinium were also included as simulation parameters (see the SI for more details regarding digital simulations and parameters used). In the simulated voltammograms, the wave at -1.12 V regains chemical reversibility, whereas the magnitude of current of the subsequent wave at −1.39 V decreases with increasing scan rate (Figure S29). These observations are consistent with the experimental voltammograms.

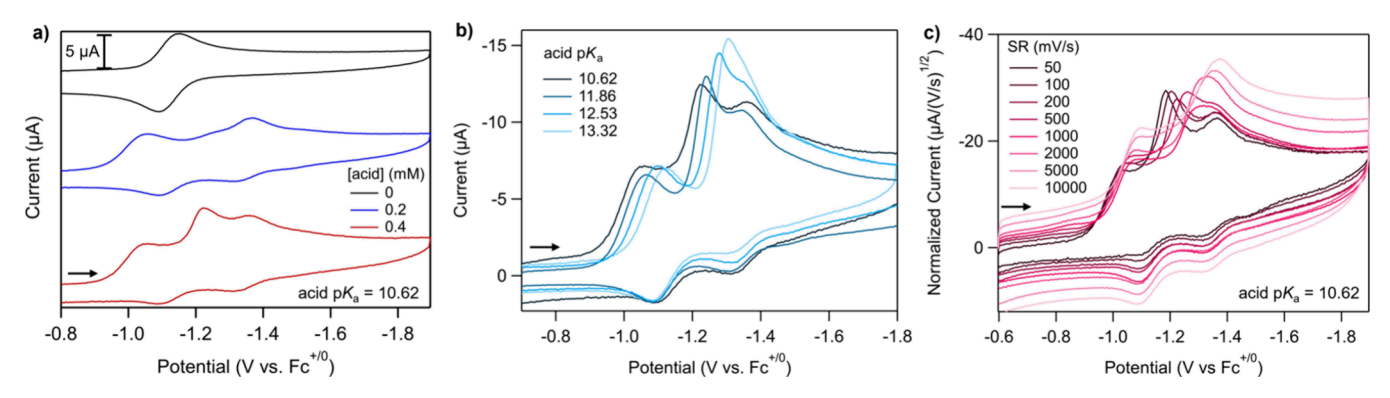


Figure 5. (a) Cyclic voltammograms of 0.2 mM $[Co^{II}py]^{2+}$ in CH_3CN with no acid (black) and with additions of 0.2 mM (blue) and 0.4 mM (red) anilinium (p K_a = 10.62). Voltammograms recorded at 200 mV/s in 0.25 M $[NBu_4][PF_6]$. (b) Cyclic voltammograms of 0.2 mM $[Co^{II}py]^{2+}$ in CH_3CN with additions of 0.4 mM anilinium (p K_a = 10.62), 4-methoxyanilinium (p K_a = 11.86), pyridinium (p K_a = 12.53), and 2-methylpyridinium (p K_a = 13.32). E_{pc} for reduction of $[Co^{II}py]^{2+}$ ranging between -1.06 and -1.12 V and that of $[Co^{II}H)py(H)]^{3+}$ ranging between -1.22 and -1.31 V. Voltammograms recorded at 200 mV/s in 0.25 M $[NBu_4][PF_6]$. (c) Cyclic voltammograms of 0.2 mM $[Co^{II}py]^{2+}$ in CH_3CN with 0.4 mM anilinium recorded at various scan rates in 0.25 M $[NBu_4][PF_6]$.

We also attempted to model the voltammograms at high acid concentrations (>2 mM) by noting that the catalytic currents may not represent the experimentally observed values given the overlap with direct acid reduction. Nevertheless, the catalytic voltammogram of [Co^{II}py]²⁺ in the presence of 10 mM 4-methoxypyridinium was successfully simulated using the same simulation parameters as those used in the low acid concentration regime (Figure S30). Notably, the experimentally observed trace crossing was also reproduced, which allowed us to probe the origin of this behavior. In the simulations, it was found that the trace crossing disappears when $k_{\rm PT2}$ or k_{Ω} is increased to more than 10^{5} and 10^{3} M⁻¹ s⁻¹, respectively. This observation suggests that the trace crossing behavior is associated with the slow kinetics of the chemical steps C2 and CH2, which impedes the subsequent reduction of $[\mathbf{Co^{II}py}]^{2+}$ (E₁) upon catalyst turnover. In this situation, $[\mathbf{Co^{II}py}]^{2+}$ is slowly generated such that the subsequent E_1 reduction does not occur until after the switching potential, giving rise to the observed high cathodic current on the reverse scan. Therefore, the more acid and time given at high acid concentrations and slow scan rates, respectively, result in additional cathodic current as more of [Co^{II}py]²⁺ is slowly generated. By increasing the reaction rate for C2 or CH2, these chemical reactions reach equilibrium faster, resulting in faster turnover and formation of [Co^{II}py]²⁺ and therefore less trace crossing. We also investigated the potential disproportion reaction between [Co^{II}py]²⁺ and [Co^{II}(H)py]⁺ to determine its impact on the observed cathodic current. However, minimal changes to the trace crossing were observed in the simulations, irrespective of the disproportion rate constant (ranging from 0 to 10⁷ M⁻¹ s⁻¹), suggesting a negligible effect.

Electrocatalytic HER in the Intermediate Acid Regime. With increasing acid strength, the voltammetric responses evolve. This is first evident in voltammograms recorded at low concentrations (0.2–0.4 mM) with organic acids with pK_a values spanning the range of 10.62–13.32. Under these conditions, the voltammograms of $[Co^{II}py]^{2+}$ exhibit both a Co(II/I) couple and the irreversible Co(III) hydride reduction wave similar to those observed in the weak acid regime (Figure 5a and Figure S11). Additionally, a new irreversible wave appears in the voltammograms at a potential intermediate between those of the Co(II/I) couple and the hydride reduction. Interestingly, the peak positions of the new

wave and the Co(II/I) couple shift more positive as the acid strength increases (Figure 5b). The cathodic peak potential shift of the Co(II/I) couple with decreasing acid pK_a is consistent with the E_1C_1 process under kinetic control because the rate constant $k_{\rm PT1}$ exhibits strong dependence on the acid pK_a (see above, Figure 3). Consistent with the weak acid regime, as the scan rate increases, the Co(II/I) couple becomes more reversible, whereas the magnitudes of current of the subsequent waves decrease (Figure 5c and Figure S12). This is accompanied by an increase in current for the direct acid reduction at more negative potentials (-1.2 to -1.6 V), and this effect is more prominent at high acid concentrations (Figures S22–S25). These results are consistent with the chemical step C_1 to form $[Co^{III}(H)py]^{2+}$ being slow and below the diffusion limit under these conditions.

The voltammograms for [Co^{II}py]²⁺ recorded with high acid concentrations (2-16 mM) exhibit catalytic waves centered at potentials positive of the [Co^{III}(H)py]²⁺ reduction (Figure 6). Notably, as the acid strength used increases, the direct acid reduction becomes more facile, and the potential associated with this event overlaps more strongly with the catalytic peaks of the molecular catalyst compared to the weak acid regime (Figures S15-S18).³² Regardless of these convoluted peaks in the catalytic region, the proton transfer rate constants $(k_{PT1}s)$ associated with hydride formation (C_1) were readily quantified using the scan rate-dependent peak shift of the Co(II/I) reduction couple (Table 1). As discussed in the weak acid regime, the rate constant k_{PT1} increases as the acid p K_a is decreased, with a constant LFER slope observed across both acid regimes (see above, Figure 3). This observation indicates that the chemical step C_1 is responsible for the observed peak potential shift. These data consequently demonstrate that initial protonation at the Co(I) center to form $[Co^{III}(H)py]^{2+}$ is also operative in this intermediate acid regime.

We considered two possible explanations for the new, intermediate redox feature observed in the voltammograms recorded at low acid concentration shown in Figure 5a. First, we hypothesized that the feature corresponded to the reduction of a protonated Co(III) hydride species, $[Co^{III}(H)-py(H)]^{3+}$, that could form via an ECCE mechanism; the first E_1C_1 step generates $[Co^{III}(H)py]^{2+}$, and the subsequent protonation forms $[Co^{III}(H)py(H)]^{3+}$ followed by the reduction of the hydride intermediate, yielding $[Co^{II}(H)py-III]^{3+}$

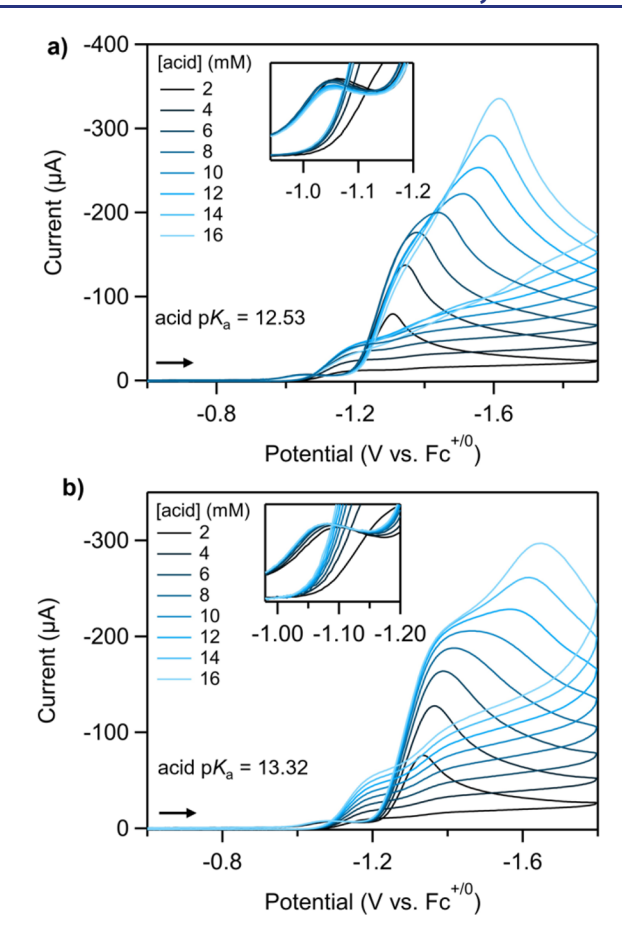


Figure 6. (a) Cyclic voltammograms of 0.2 mM $[{\bf Co^I py}]^{2+}$ in CH₃CN with additions of 2–16 mM pyridinium (p K_a = 12.53). (b) Cyclic voltammograms of 0.2 mM $[{\bf Co^I py}]^{2+}$ in CH₃CN with additions of 2–16 mM 2-methylpyridinium (p K_a = 13.32). Voltammograms recorded at 200 mV/s in 0.25 M $[{\rm NBu_4}][{\rm PF_6}]$. Insets: shifts of Co(II/I) reduction couple as a function of acid concentration.

(H)]²⁺. The reduction observed at ca. -1.22 to -1.31 V would thus correspond to the reduction of $[\mathbf{Co^{III}(H)py(H)}]^{3+}$. Second, we hypothesized that this feature is reflective of total catalysis (zone KT2).³⁹ In zone KT2, we would expect that the small amount of Co(III) hydride reduced at potentials positive of $E^{\circ\prime}([\mathbf{Co^{III}(H)py}]^{2+/+})$ is sufficient to react with all acid in the reaction—diffusion layer as the catalyst turns over. The intermediate feature at ca. -1.22 to -1.31 V thus corresponds to catalysis, whereas the second feature at -1.39 V is the reduction of $[\mathbf{Co^{III}(H)py}]^{2+}$ without additional acid to react with and turn over.

Digital simulations were used to test these hypotheses under low acid concentrations (0.2–0.4 mM). For the ECEC mechanism, the $k_{\rm PT1}$ values were taken from the peak shift analysis, and the $k_{\rm PT2}$ values were arbitrarily set to be an order of magnitude higher than $k_{\rm PT1}$ to take into account the more facile kinetics of the C_2 process than that of C_1 (as done above). The intermediate redox feature of the voltammograms is readily simulated with the ECEC mechanism presented above (Figures S31–S38). Concentration profiles of reactants and intermediates produced from the digital simulation software indicate that at low acid concentrations, the acid is depleted prior to complete reduction of $[\mathbf{Co^{II}(H)py}]^{2+}$ such that only a fraction of the $[\mathbf{Co^{II}(H)py}]^{+}$ formed can turn over

catalytically, consistent with zone KT2. By contrast, digital simulations of the ECCE mechanism that would proceed through a $[\mathbf{Co^{III}(H)py(H)}]^{3+}$ intermediate are unable to reproduce the intermediate redox feature with rate constants for protonating $[\mathbf{Co^{III}(H)py}]^{2+}$ ranging from 0 to $10^{10}~\mathrm{M^{-1}~s^{-1}}$. Together, digital simulations support that HER proceeds through the same ECEC mechanism that occurs with weaker acids, and at low acid concentrations, the voltammetric response corresponds to zone KT2.

Digital simulations were further used to rationalize the position of the intermediate redox feature observed at low concentrations of acid (shown for 0.2–0.4 mM), ranging from ca. -1.22 to -1.31 V. At a constant scan rate, the peak becomes more positive with stronger acids as shown in Figure 5b. This acid p $K_{\rm a}$ dependent behavior of the peak potential is also reproduced by digital simulations (Figure S40) and reflects the larger rate constants and $K_{\rm eq}$ values for the C_2 step observed for stronger acids, which lead to faster catalyst turnover and more rapid consumption of the acid. This explains why the intermediate redox feature originating from zone KT2 is observed in this acid regime and not in the weaker acid regime, although HER proceeds through the same ECEC mechanism in both acid regimes.

The voltammograms of $[\mathbf{Co^{II}py}]^{2+}$ recorded with high acid concentrations (>2 mM) exhibit trace crossing analogous to the weak acid regime (Figures S22 - S25). The trace crossing was reproduced by simulating the voltammograms of $[\mathbf{Co^{II}py}]^{2+}$ in the presence of 20 mM of anilinium with simulation parameters used in the low acid concentration regime (Figure S39). Similar to the weak acid regime, the trace crossing vanishes when k_{Ω} is increased to more than 10^3 M $^{-1}$ s $^{-1}$. In this case, the trace crossing may primarily originate from the slow chemical step C_{H2} . The slow release of H_2 impedes the reduction of $[\mathbf{Co^{II}py}]^{2+}$ (E1), which gives rise to the cathodic current in the reverse scan, as demonstrated in the weak acid regime.

Electrocatalytic HER in the Strong Acid Regime. Voltammograms for $[\mathbf{Co^{II}py}]^{2+}$ recorded with 2,6-dichloroanilinium (p $K_a=5.06$) (0.2–0.4 mM), the strongest acid explored in this study, exhibit similar irreversible events as observed for weak and intermediate acids along with a new irreversible wave at a slightly more positive potential ($E_{\rm pc}=-0.99~\rm V$) (Figure 7a). Furthermore, as acid concentration increases from 0.8 to 4 mM, catalytic currents are observed to emerge from the most anodic peaks, exhibiting peak potentials less than $-0.99~\rm V$ at a scan rate of 200 mV/s (Figure 7b). These observations suggest a new reaction pathway in addition to those accessible with weaker acids.

First, we recognize that with 2,6-dichloroanilinium, a fraction of $[\mathbf{Co^{II}py}]^{2+}$ can be protonated to form $[\mathbf{Co^{II}py}(\mathbf{H})]^{3+}$ (C₃), and the new irreversible wave is assigned as the reduction of this species to generate $[\mathbf{Co^{II}py}(\mathbf{H})]^{2+}$ (E₃). This assignment is consistent with the pK_a value of 6.8 for $[\mathbf{Co^{II}py}(\mathbf{H})]^{3+}$ and the partial protonation reaction of $[\mathbf{Co^{II}py}]^{2+}$ by 2,6-dichloroanilinium prior to reduction as observed by ${}^{1}\mathbf{H}$ NMR spectroscopy (*vide supra*). The partial protonation of $[\mathbf{Co^{II}py}]^{2+}$ at low acid conditions explains why the reduction events E₁, E₂, and E₃ are observable in the voltammograms recorded at 0.2 and 0.4 mM 2,6-dichloroanilinium (Figure 7a). The triply charged $[\mathbf{Co^{II}py}(\mathbf{H})]^{3+}$ is easier to reduce than the doubly charged $[\mathbf{Co^{II}py}(\mathbf{H})]^{3+}$, which explains the more positive reduction potential of the former species ($E_{pc} = -0.99$ V vs $E_{1/2} = -1.12$ V). We hypothesize

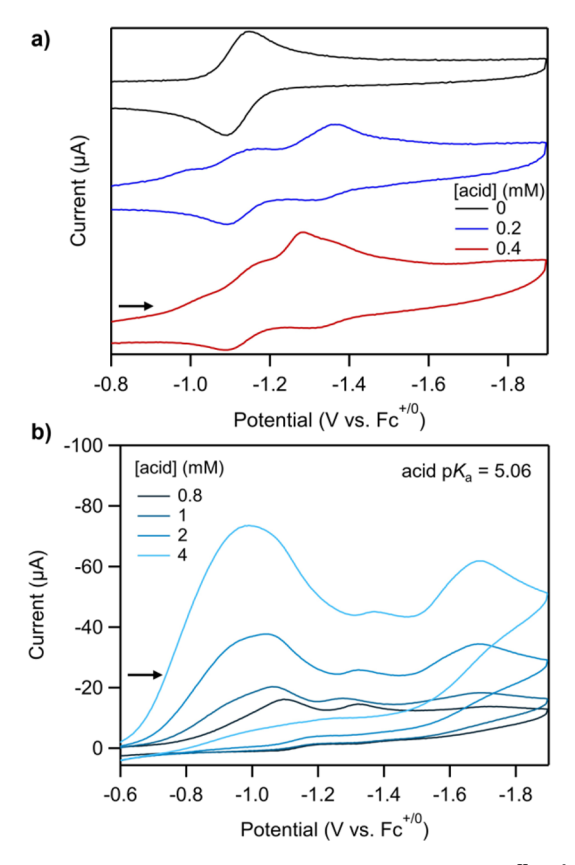


Figure 7. (a) Cyclic voltammograms of 0.2 mM $[Co^{II}py]^{2+}$ in CH₃CN with no acid (black) and with additions of 0.2 mM (blue) and 0.4 mM (red) 2,6-dichloroanilinium (pK₄ = 5.06). (b) Cyclic voltammograms of 0.2 mM $[Co^{II}py]^{2+}$ in CH₃CN with additions of 0.8–4 mM 2,6-dichloroanilinium. Voltammograms recorded at 200 mV/s in 0.25 M $[NBu_4][PF_6]$.

that the reduction of $[Co^{II}py(H)]^{3+}$ to form $[Co^{I}py(H)]^{2+}$ (E₃) is followed by rapid tautomerization (C_{taut}), generating the hydride species $[Co^{III}(H)py]^{2+}$ (Scheme 5)

An increase in cathodic current with increasing acid concentration indicates catalytic acid reduction associated with the formation of $[\mathbf{Co^{III}(H)py}]^{2+}$ (which can be formed by the E_1C_1 and C_3E_3 mechanisms) (Figure 7b). We hypothesize that direct protonation of the hydride with strong acids can liberate H_2 and $[\mathbf{Co^{III}(py)}]^{3+}$, which would be rapidly reduced at these negative potentials to regenerate $[\mathbf{Co^{II}(py)}]^{2+}$, completing the catalytic cycle (Scheme 6). Note that these additional pathways are likely not operative in the stochiometric reactions between $[\mathbf{Co^Ipy}]^+$ and acids and the CPE experiments described above as the acids used are not sufficiently strong to protonate the hydride species $[\mathbf{Co^{III}(H)-py}]^{2+}$. However, with 2,6-dichloroanilinium, the hydride

reduction/protonation mechanisms likely operate in parallel given the observed peaks corresponding to the reductions of $[Co^{II}(py)]^{2+}$ and $[Co^{III}(H)py]^{2+}$ at more negative potentials. Note that 2,6-dichloroanilinium is directly reduced at the electrode, giving rise to the enhanced current at ca. – 1.6 V (Figure 7b and Figure S19).

To support these mechanistic hypotheses, digital simulations were carried out to introduce two new mechanistic sequences that occur in parallel to the $E_1C_1E_2C_2$ mechanism introduced above: a C_3E_3 pathway followed by tautomerization (C_{taut}) to form $[\textbf{Co}^{III}(\textbf{H})\textbf{py}]^{2+}$ and a protonation of $[\textbf{Co}^{III}(\textbf{H})\textbf{py}]^{2+}$ (formed by either the C_3E_3 pathway or the E_1C_1 pathway) to release H_2 and form $[\textbf{Co}^{III}\textbf{py}]^{3+}$ (C_{H2_2}) followed by reduction of $[Co^{III}py]^{3+}$ (E₄). Given the acid strength of 2,6dichloroanilinium (p $K_a = 5.06$), $k_{\rm PT1}$ and $k_{\rm PT2}$ likely reach the diffusion limit (up to $10^{10}~{\rm M}^{-1}~{\rm s}^{-1}$). This assumption is supported by the $k_{\rm PT1}$ value of 6.2×10^{13} estimated by extrapolating the trend of the LFER plot (see above, Figure 3) and the fact that k_{PT2} is known to be slightly higher than k_{PT1} . The K_{eq} value for C_3 is set based on the relative pK_a values of $[Co^{II}py(H)]^{3+}$ and 2,6-dichloroanilinium. To achieve rapid protonation equilibrium, the rate constant for C_3 (k_{PT3}) is set at the diffusion limit, which is $1.0 \times 10^{10} \text{ M}^{-1} \text{ s}^{-1}$. The reduction potential of $[Co^{II}py(H)]^{3+}$ is estimated to be -0.99V based on the experimentally observed E_{pc} of the new reduction feature.

With this model, the appearance of a new voltammetric feature attributed to the $[Co^{II}py(H)]^{3+}$ reduction is successfully simulated across acid concentrations of 0.8-4 mM (Figure S43). Moreover, a catalytic wave centered at ca. -0.99V is observed. Simulations of the voltammograms observed experimentally in Figure 7b are achieved when the rate constant of $C_{H2\ 2}\ (k_{\gamma})$ is on the order of $10^5\ M^{-1}\ s^{-1}$ (Figure S42). To further probe the origin of the catalytic wave preceding the [Co^{fi}py]²⁺ reduction, the C₃E₃ process was removed from the simulations. This allows the hydride species $[\mathbf{Co^{III}(H)py}]^{2+}$, generated from the E_1C_1 process, to engage in catalysis through the hydride protonation and reduction pathways. The catalytic wave remained present at approximately -0.99 V even without the C_3E_3 process (Figure S41). However, the peak position shifted to a more positive potential, similar to that observed experimentally with the C₃E₃ process included. These results demonstrate that the observed catalysis involves the protonation of the hydride intermediate $[Co^{III}(H)py]^{2+}$ generated from both the C_3E_3 and E₁C₁ pathways. Collectively, these experiments and simulations support the conclusion that a C₃E₃ tautomerization pathway to access [Co^{III}(H)py]²⁺ can occur with strong acids and that $[Co^{III}(H)py]^{2+}$ protonation to release H₂ can also occur with strong acids (Scheme 6).

Scheme 5. Proposed Mechanism for the Formation of $[Co^{III}py(H)]^{2+}$ in the Strong Acid Regime

Scheme 6. Proposed Parallel ECEC and CECCE Mechanisms to Release H₂ in the Strong Acid Regime

$$\begin{bmatrix} \text{Co}^{\text{II}}(\textbf{H})\text{py} \end{bmatrix}^{2+} \\ \text{C}_{2} \\ \text{[Co}^{\text{II}}(\textbf{H})\text{py}(\textbf{H})]^{2+} \\ \text{C}_{12} \\ \text{C}_{12} \\ \text{C}_{12} \\ \text{C}_{12} \\ \text{E}_{2} \\ \text{C}_{12} \\ \text{E}_{2} \\ \text{C}_{12} \\ \text{E}_{3} \\ \text{C}_{13} \\ \text{C}_{14} \\ \text{E}_{1} \\ \text{C}_{15} \\ \text{E}_{1} \\ \text{C}_{15} \\ \text{E}_{1} \\ \text{C}_{15} \\ \text{E}_{1} \\ \text{C}_{15} \\ \text{C}_{1$$

Scheme 7. Thermochemical Cycles Relating Catalytic HER Intermediates

"Values in red and blue are pK_a and reduction potential, respectively. Italicized reduction potential values are estimated from either E_{pc} or $E_{1/2}$ at a fast scan rate. Italicized pK_a values are either estimated from digital simulations or averaged from a range of pK_a values. The number in parentheses is calculated using Hess's law. Chemical species and reactions in gray were not observed in this study.

Thermochemical Parameters Associated with Proposed HER Intermediates. The electrochemical studies as well as the stochiometric reactivity of [Co^{II}py]²⁺ with a range of acids spanning 20 pK_a units in acetonitrile enable the construction of thermochemical cycles relating key intermediates in the catalytic HER mechanisms proposed herein (Scheme 7). Although some of the chemical steps were not observed in this study, the thermochemical cycles allow us to determine their associated thermochemical parameters. For example, the pK_a value associated with the ligand protonation species $[Co^{I}py(H)]^{2+}$ (C₄) was calculated to be about 9.0 via Hess's law (see the SI). However, note that the reduction step E₃ is irreversible, and therefore, the thermochemical value is taken from the peak potentials E_{pc} . The reduction potential of the E_2 process was estimated from the $E_{1/2}$ value of the voltammogram of 0.2 mM [Co^{II}py]²⁺ with 0.2 mM 4methoxypyridinium recorded at a scan rate of 10,000 mV/s, where the reversibility of the event was recovered (Figure 2b). Additionally, the pK_a value for steps C_1 and C_2 were taken from the average value of the estimated pK_a range and digital simulations, respectively, because the reactive nature of these hydride intermediates prevents the determination of the exact pK_a values. Nevertheless, these thermodynamic cycles help us understand the energetics of the elementary steps constituting the catalytic cycles and demonstrate that the choice of acid and applied potential has a direct impact on the accessible HER mechanism. Notably, the metal-based protonation to form $[Co^{III}(H)py]^{2+}$ (C₁) is found to be both thermodynamically and kinetically more accessible than the ligand-based protonation of $[\mathbf{Co^Ipy}]^+$ (C₄). The kinetically accessible direct metal protonation is attributed to the relatively low structural reorganization to directly protonate the cobalt center, which is in agreement with our structural analysis of [Co¹py]⁺.

CONCLUDING REMARKS

This report provides detailed mechanistic and kinetic analyses of the electrocatalytic HER activity of the [Co^{II}py]²⁺ complex supported by a polypyridyl ligand bearing a pendant pyridyl base. The reduced species [Co^Ipy]⁺ was isolated and characterized as a five-coordinate, low-spin complex. This complex is capable of reducing protons to H₂ via a homolytic reaction of a Co(III) hydride intermediate. The structural rigidity and limited electronic changes upon forming the hydride intermediate suggest that the intrinsic barrier to directly protonate the Co(I) center is relatively small. Consistently, electrochemical measurements under catalytic conditions support the formation of the Co(III) hydride intermediate via direct metal protonation despite the presence of the pendant base, which is typically observed as a more kinetically accessible protonation site. The metal-based protonation to generate the hydride intermediate is therefore both kinetically and thermodynamically more accessible than the ligand-based protonation. Our findings support the broad hypothesis that kinetic barriers to direct metal protonation are correlated with the geometric and electronic rearrangements required to form metal hydride intermediates. More importantly, we demonstrate that such barriers can be minimized by judicious ligand design. This work provides a strategy for realizing the efficient formation of metal hydride intermediates in HER catalysis, which may be applicable to other fuel-forming reactions (e.g., N2 reduction, CO2 reduction) involving metal hydride intermediates.

The reactivity of $[\mathbf{Co^{II}py}]^{2+}$ with a series of organic acids in acetonitrile was investigated under electrochemical conditions. We found that the choice of proton source impacts on the accessible electrocatalytic HER mechanisms. When using acids with pK_a values ranging from 10.62 to 14.47, an ECEC pathway is operative through a Co(III) hydride intermediate

generated from the first EC process. In this acid regime, an acid-independent behavior was observed at high acid concentrations, which was assigned to the rate-limiting H-H bond formation or release of H2 from a doubly protonated cobalt species formed in the second EC step. Although the voltammetric responses with acid pKa ranging from 10.62 to 13.32 are distinct from weaker acids at low acid concentrations, we show that these changes arise from total catalysis (zone KT2), yet the operating mechanism remains unchanged. An LFER correlating rate constants for the first protonation step with the acid pK_a values was observed across both acid regimes, supporting the assignment that the formation of the Co(III) hydride is a common mechanistic step. As the acid p K_a decreases to 5.06 in the strong acid regime, [Co^{II}py]²⁺ is protonated at the pendant pyridine prior to electron transfer, following an CE pathway. Furthermore, $[Co^{III}(H)py]^{2+}$ can be protonated directly to evolve H₂ with this strong acid. Notably, the mechanistic assignments allow us to determine appropriate methods (i.e., current plateau analysis, peak-shift analysis, and digital simulations) to quantify kinetic parameters associated with the catalytic elementary steps. The determination of thermodynamic parameters (i.e., pK_a values) of the catalytic intermediates is also essential, as some of the kinetic parameters are highly dependent on the reaction driving forces. The synergy of thermodynamics and kinetics demonstrated in this work indicates that these parameters should not be considered separately, especially when optimizing the performance of electrocatalysts. Together, these analyses provide a complete description of the catalytic system and offer opportunities to control and fine-tune the kinetics of charge transfer through a deep understanding of each and every elementary step.

ASSOCIATED CONTENT

Supporting Information

The Supporting Information is available free of charge at https://pubs.acs.org/doi/10.1021/jacs.3c10408.

> Experimental details including synthesis, characterization, reactivity studies, electrochemical measurements, digital simulations, and thermochemical calculations (PDF)

Accession Codes

CCDC 2296282 contains the supplementary crystallographic data for this paper. These data can be obtained free of charge via www.ccdc.cam.ac.uk/data_request/cif, or by emailing data request@ccdc.cam.ac.uk, or by contacting The Cambridge Crystallographic Data Centre, 12 Union Road, Cambridge CB2 1EZ, UK; fax: +44 1223 336033.

AUTHOR INFORMATION

Corresponding Author

Jillian L. Dempsey - Department of Chemistry, University of North Carolina at Chapel Hill, Chapel Hill, North Carolina 27599-3290, United States; o orcid.org/0000-0002-9459-4166; Email: dempseyj@email.unc.edu

Authors

Jaruwan Amtawong – Department of Chemistry, University of North Carolina at Chapel Hill, Chapel Hill, North Carolina 27599-3290, United States

- Charlotte L. Montgomery Department of Chemistry, University of North Carolina at Chapel Hill, Chapel Hill, North Carolina 27599-3290, United States
- Gabriella P. Bein Department of Chemistry, University of North Carolina at Chapel Hill, Chapel Hill, North Carolina 27599-3290, United States; o orcid.org/0000-0003-1970-
- **Austin L. Raithel** Department of Chemistry, Michigan State University, East Lansing, Michigan 48824, United States
- Thomas W. Hamann Department of Chemistry, Michigan State University, East Lansing, Michigan 48824, United States; orcid.org/0000-0001-6917-7494
- Chun-Hsing Chen Department of Chemistry, University of North Carolina at Chapel Hill, Chapel Hill, North Carolina 27599-3290, United States; o orcid.org/0000-0003-0150-

Complete contact information is available at: https://pubs.acs.org/10.1021/jacs.3c10408

Author Contributions

All authors have given approval to the final version of the manuscript.

Notes

The authors declare no competing financial interest.

ACKNOWLEDGMENTS

This work was primarily supported by the U.S. Department of Energy, Office of Science, Office of Basic Energy Sciences, under Award DE-SC0015303 (electrochemical measurements, reactivity studies, and data analysis) and Award DE-SC0017342 (synthesis of [Co^{II}py²⁺]). We acknowledge the use of gas chromatography in the CHASE Instrumentation Facility established by the Center for Hybrid Approaches in Solar Energy to Liquid Fuels, CHASE, an Energy Innovation Hub funded by the US Department of Energy, Office of Basic Energy Sciences, Office of Science, under award DE-SC0021173. We thank the University of North Carolina's Department of Chemistry NMR Core Laboratory for their use of their NMR spectrometers, supported by the National Science Foundation under Grant CHE-0922858. We acknowledge the University of North Carolina at Chapel Hill Department of Chemistry Mass Spectrometry Core Laboratory, supported by the National Science Foundation under Grant CHE-1726291. Structure determination via X-ray crystallography is supported by the National Science Foundation under Grant CHE-2117287.

REFERENCES

- (1) Turner, J. A. Sustainable Hydrogen Production. Science 2004, 305 (5686), 972-974.
- (2) Lewis, N. S.; Nocera, D. G. Powering the Planet: Chemical Challenges in Solar Energy Utilization. Proc. Natl. Acad. Sci. U. S. A. 2006, 103 (43), 15729-15735.
- (3) Walter, M. G.; Warren, E. L.; McKone, J. R.; Boettcher, S. W.; Mi, Q.; Santori, E. A.; Lewis, N. S. Solar Water Splitting Cells. Chem. Rev. 2010, 110 (11), 6446-6473.
- (4) Tran, P. D.; Artero, V.; Fontecave, M. Water Electrolysis and Photoelectrolysis on Electrodes Engineered Using Biological and Bio-Inspired Molecular Systems. Energy Environ. Sci. 2010, 3 (6), 727.
- (5) Zhu, J.; Hu, L.; Zhao, P.; Lee, L. Y. S.; Wong, K.-Y. Recent Advances in Electrocatalytic Hydrogen Evolution Using Nanoparticles. Chem. Rev. 2020, 120 (2), 851-918.

- (6) Esswein, A. J.; Nocera, D. G. Hydrogen Production by Molecular Photocatalysis. *Chem. Rev.* **2007**, *107* (10), 4022–4047.
- (7) Kumar, A.; Daw, P.; Milstein, D. Homogeneous Catalysis for Sustainable Energy: Hydrogen and Methanol Economies, Fuels from Biomass, and Related Topics. *Chem. Rev.* **2022**, *122* (1), 385–441.
- (8) Zee, D. Z.; Chantarojsiri, T.; Long, J. R.; Chang, C. J. Metal—Polypyridyl Catalysts for Electro- and Photochemical Reduction of Water to Hydrogen. *Acc. Chem. Res.* **2015**, 48 (7), 2027–2036.
- (9) Droghetti, F.; Lucarini, F.; Molinari, A.; Ruggi, A.; Natali, M. Recent Findings and Future Directions in Photosynthetic Hydrogen Evolution Using Polypyridine Cobalt Complexes. *Dalton Trans.* **2022**, *51* (28), 10658–10673.
- (10) Bigi, J. P.; Hanna, T. E.; Harman, W. H.; Chang, A.; Chang, C. J. Electrocatalytic Reduction of Protons to Hydrogen by a Water-Compatible Cobalt Polypyridyl Platform. *Chem. Commun.* **2010**, *46* (6), 958–960.
- (11) Schnidrig, S.; Bachmann, C.; Müller, P.; Weder, N.; Spingler, B.; Joliat-Wick, E.; Mosberger, M.; Windisch, J.; Alberto, R.; Probst, B. Structure-Activity and Stability Relationships for Cobalt Polypyridyl-Based Hydrogen-Evolving Catalysts in Water. *ChemSusChem* **2017**, *10* (22), 4570–4580.
- (12) Sun, Y.; Sun, J.; Long, J. R.; Yang, P.; Chang, C. J. Photocatalytic Generation of Hydrogen from Water Using a Cobalt Pentapyridine Complex in Combination with Molecular and Semiconductor Nanowire Photosensitizers. *Chem. Sci.* **2013**, *4* (1), 118–124
- (13) Khnayzer, R. S.; Thoi, V. S.; Nippe, M.; King, A. E.; Jurss, J. W.; El Roz, K. A.; Long, J. R.; Chang, C. J.; Castellano, F. N. Towards a Comprehensive Understanding of Visible-Light Photogeneration of Hydrogen from Water Using Cobalt(II) Polypyridyl Catalysts. *Energy Env. Sci.* **2014**, *7* (4), 1477–1488.
- (14) Queyriaux, N.; Sun, D.; Fize, J.; Pécaut, J.; Field, M. J.; Chavarot-Kerlidou, M.; Artero, V. Electrocatalytic Hydrogen Evolution with a Cobalt Complex Bearing Pendant Proton Relays: Acid Strength and Applied Potential Govern Mechanism and Stability. *J. Am. Chem. Soc.* **2020**, *142* (1), 274–282.
- (15) Singh, W. M.; Baine, T.; Kudo, S.; Tian, S.; Ma, X. A. N.; Zhou, H.; DeYonker, N. J.; Pham, T. C.; Bollinger, J. C.; Baker, D. L.; Yan, B.; Webster, C. E.; Zhao, X. Electrocatalytic and Photocatalytic Hydrogen Production in Aqueous Solution by a Molecular Cobalt Complex. *Angew. Chem., Int. Ed.* **2012**, *51* (24), 5941–5944.
- (16) Tong, L.; Zong, R.; Thummel, R. P. Visible Light-Driven Hydrogen Evolution from Water Catalyzed by A Molecular Cobalt Complex. J. Am. Chem. Soc. 2014, 136 (13), 4881–4884.
- (17) Zhang, P.; Wang, M.; Gloaguen, F.; Chen, L.; Quentel, F.; Sun, L. Electrocatalytic Hydrogen Evolution from Neutral Water by Molecular Cobalt Tripyridine—Diamine Complexes. *Chem. Commun.* **2013**, *49* (82), 9455.
- (18) Singh, W. M.; Mirmohades, M.; Jane, R. T.; White, T. A.; Hammarström, L.; Thapper, A.; Lomoth, R.; Ott, S. Voltammetric and Spectroscopic Characterization of Early Intermediates in the Co(II)—Polypyridyl-Catalyzed Reduction of Water. *Chem. Commun.* **2013**, 49 (77), 8638.
- (19) Deponti, E.; Luisa, A.; Natali, M.; Iengo, E.; Scandola, F. Photoinduced Hydrogen Evolution by a Pentapyridine Cobalt Complex: Elucidating Some Mechanistic Aspects. *Dalton Trans* **2014**, *43* (43), 16345–16353.
- (20) Roubelakis, M. M.; Bediako, D. K.; Dogutan, D. K.; Nocera, D. G. Proton-Coupled Electron Transfer Kinetics for the Hydrogen Evolution Reaction of Hangman Porphyrins. *Energy Environ. Sci.* **2012**, *5* (7), 7737.
- (21) Roubelakis, M. M.; Bediako, D. K.; Dogutan, D. K.; Nocera, D. G. Influence of the Proton Relay Spacer on Hydrogen Electrocatalysis by Cobalt Hangman Porphyrins. *J. Porphyr. Phthalocyanines* **2021**, 25 (07n08), 714–723.
- (22) Montgomery, C. L.; Amtawong, J.; Jordan, A. M.; Kurtz, D. A.; Dempsey, J. L. Proton Transfer Kinetics of Transition Metal Hydride Complexes and Implications for Fuel-Forming Reactions. *Chem. Soc. Rev.* 2023, 52, 7137–7169.

- (23) Rountree, E. S.; Dempsey, J. L. Potential-Dependent Electrocatalytic Pathways: Controlling Reactivity with pK_a for Mechanistic Investigation of a Nickel-Based Hydrogen Evolution Catalyst. *J. Am. Chem. Soc.* **2015**, *137* (41), 13371–13380.
- (24) Wiedner, E. S.; Brown, H. J. S.; Helm, M. L. Kinetic Analysis of Competitive Electrocatalytic Pathways: New Insights into Hydrogen Production with Nickel Electrocatalysts. *J. Am. Chem. Soc.* **2016**, *138* (2), 604–616.
- (25) Raithel, A. L.; Meador, W. E.; Kim, T.-Y.; Staples, R. J.; Delcamp, J. H.; Hamann, T. W. Molecular Switch Cobalt Redox Shuttle with a Tunable Hexadentate Ligand. *J. Am. Chem. Soc.* **2023**, 145 (2), 1367–1377.
- (26) Elgrishi, N.; Kurtz, D. A.; Dempsey, J. L. Reaction Parameters Influencing Cobalt Hydride Formation Kinetics: Implications for Benchmarking H₂-Evolution Catalysts. *J. Am. Chem. Soc.* **2017**, *139* (1), 239–244.
- (27) Wiedner, E. S.; Bullock, R. M. Electrochemical Detection of Transient Cobalt Hydride Intermediates of Electrocatalytic Hydrogen Production. *J. Am. Chem. Soc.* **2016**, *138* (26), 8309–8318.
- (28) Rountree, E. S.; Martin, D. J.; McCarthy, B. D.; Dempsey, J. L. Linear Free Energy Relationships in the Hydrogen Evolution Reaction: Kinetic Analysis of a Cobaloxime Catalyst. *ACS Catal.* **2016**, *6* (5), 3326–3335.
- (29) Addison, A. W.; Rao, T. N.; Reedijk, J.; van Rijn, J.; Verschoor, G. C. Synthesis, Structure, and Spectroscopic Properties of Copper(II) Compounds Containing Nitrogen-Sulphur Donor Ligands; the Crystal and Molecular Structure of Aqua[1,7-bis(N-Methylbenzimidazol-2'-yl)-2,6-Dithiaheptane]Copper(II) Perchlorate. J. Chem. Soc., Dalton Trans. 1984, 1349–1356.
- (30) Kaljurand, I.; Kütt, A.; Sooväli, L.; Rodima, T.; Mäemets, V.; Leito, I.; Koppel, I. A. Extension of the Self-Consistent Spectrophotometric Basicity Scale in Acetonitrile to a Full Span of 28 pK_a Units: Unification of Different Basicity Scales. *J. Org. Chem.* **2005**, 70 (3), 1019–1028.
- (31) Kurtz, D. A.; Dhar, D.; Elgrishi, N.; Kandemir, B.; McWilliams, S. F.; Howland, W. C.; Chen, C.-H.; Dempsey, J. L. Redox-Induced Structural Reorganization Dictates Kinetics of Cobalt(III) Hydride Formation via Proton-Coupled Electron Transfer. *J. Am. Chem. Soc.* **2021**, *143* (9), 3393–3406.
- (32) McCarthy, B. D.; Martin, D. J.; Rountree, E. S.; Ullman, A. C.; Dempsey, J. L. Electrochemical Reduction of Brønsted Acids by Glassy Carbon in Acetonitrile—Implications for Electrocatalytic Hydrogen Evolution. *Inorg. Chem.* **2014**, 53 (16), 8350–8361.
- (33) McCarthy, B. D.; Dempsey, J. L. Decoding Proton-Coupled Electron Transfer with Potential–pK_a Diagrams. *Inorg. Chem.* **2017**, 56 (3), 1225–1231.
- (34) Rountree, E. S.; McCarthy, B. D.; Dempsey, J. L. Decoding Proton-Coupled Electron Transfer with Potential— pK_a Diagrams: Applications to Catalysis. *Inorg. Chem.* **2019**, 58 (10), 6647–6658.
- (35) Savéant, J.-M. Elements of Molecular and Biomolecular Electrochemistry; John Wiley & Sons, Inc.: Hoboken, NJ, 2019 pp 78 180 DOI: 10.1002/9781119292364.
- (36) Shi, S.; Daniels, L. M.; Espenson, J. H. Molecular Structure of a Cobalt(I) Complex Lacking a Carbonyl Ligand. A Unique Example of Cobalt-Nitrogen Bond Shortening. *Inorg. Chem.* **1991**, 30 (18), 3407–3410.
- (37) Rountree, E. S.; McCarthy, B. D.; Eisenhart, T. T.; Dempsey, J. L. Evaluation of Homogeneous Electrocatalysts by Cyclic Voltammetry. *Inorg. Chem.* **2014**, 53 (19), 9983–10002.
- (38) Costentin, C.; Savéant, J.-M. Multielectron, Multistep Molecular Catalysis of Electrochemical Reactions: Benchmarking of Homogeneous Catalysts. *ChemElectroChem.* **2014**, *1* (7), 1226–1236.
- (39) Martin, D. J.; McCarthy, B. D.; Rountree, E. S.; Dempsey, J. L. Qualitative Extension of the EC' Zone Diagram to a Molecular Catalyst for a Multi-Electron, Multi-Substrate Electrochemical Reaction. *Dalton Trans.* **2016**, 45 (24), 9970–9976.